

# Near-deterministic activation of room temperature quantum emitters in hexagonal boron nitride: supplementary material

NICHOLAS V. PROSCIA<sup>1,2,#</sup>, ZAV SHOTAN<sup>1,#</sup>, HARISHANKAR JAYAKUMAR<sup>1</sup>, PRITHVI REDDY<sup>3</sup>, CHARLES COHEN<sup>1</sup>, MICHAEL DOLLAR<sup>1</sup>, AUDRIUS ALKAUSKAS<sup>4</sup>, MARCUS DOHERTY<sup>3</sup>, CARLOS A. MERILES<sup>1,2,\*</sup> & VINOD M. MENON<sup>1,2,\*</sup>

<sup>1</sup>Dept. of Physics, City College of New York, New York, USA

<sup>2</sup>Dept. of Physics, Graduate Center of the City University of New York (CUNY), USA

<sup>3</sup>Laser Physics Centre, Research School of Physics and Engineering, Australian National University, Canberra, Australia

<sup>4</sup>Center for Physical Science and Technology, Vilnius, Lithuania

\* Corresponding authors: [cmeriles@ccny.cuny.edu](mailto:cmeriles@ccny.cuny.edu), [vmenon@ccny.cuny.edu](mailto:vmenon@ccny.cuny.edu)

Published 14 September 2018

This document provides supplementary information to “Near-deterministic activation of room temperature quantum emitters in hexagonal boron nitride,” <https://doi.org/10.1364/OPTICA.5.001128>. The supplementary material consists of three sections: The first section discusses the experimental methods and additional sample characterizations as well as information related to time-correlation measurements and statistical analysis. The second section details photonic effects due to the SiO<sub>2</sub> pillars via FEM simulations. The third section discusses the deformation potential calculations due to deformation of the hBN film.

## 1. Experimental methods

**Substrate and sample preparation.** The silica nano-pillars were made by masked etching of a 300 nm thick thermal oxide layer on a Si wafer via electron beam lithography. The desired geometry of the SiO<sub>2</sub> pillars was first written into a 300 nm layer of negative resist (Ma-N 2403) on top of the thermal oxide wafer via electron beam lithography (Eliox ELS-G100). Then, after development in MIF 726, deep reactive ion etching (DRIE) was utilized to anisotropically etch the patterned wafer. The polymerized resist masks the SiO<sub>2</sub> layer from the etchant gas (CHF<sub>3</sub>) and enables the SiO<sub>2</sub> pillars to form from the protected silica. Finally, the excess resist is removed via a two-step process; first the majority of the resist is dissolved by the solvent Remover PG and then the pillar substrate is subjected to an O<sub>2</sub> plasma for 10 minutes to fully remove any leftover resist. It was found that the O<sub>2</sub> plasma etches the silica further ~15 nm, which is attributed to contaminants present on the DRIE chamber walls.

The hBN sample studied herein was purchased from Graphene Supermarket as a 20-nm-thick flake, grown by CVD on a 25- $\mu$ m-thick Cu substrate. The flake was transferred to the patterned silica wafer by a Poly(methyl methacrylate) (PMMA) transfer method [1]. First, a 200 nm layer of PMMA was spin coated onto the h-BN/Cu substrate. After a 90 s prebake at 180 °C, the Cu substrate was removed in a bath of ferric chloride at 60 °C. The hBN/PMMA film was then placed in a Radio Corporation of America (RCA) 2 bath to remove any excess Cu and subsequently in a RCA 1 bath to remove any organic impurities. After rinsing with DI water, the film was lifted from the water bath with a nanopillar sample and allowed to dry. The sample was then heated to 180 °C for 20 minutes to remove any trapped gas and subsequently placed in an acetone bath for 90 minutes at 52 °C to remove the majority of the PMMA film.

The pillar substrates were patterned in arrays with various pillar diameters, which ranged from 75 nm to 2  $\mu$ m, and varying

itches, from 2  $\mu\text{m}$  to 6  $\mu\text{m}$ . We found that the h-BN was supported by the pillars for pillar heights below  $\sim 155$  nm while pillars with heights above 155 nm showed evidence the h-BN was pierced by the pillars. We also find that a 2  $\mu\text{m}$  pitch is a sufficient distance to allow the h-BN to drape over the pillar and contact the substrate between pillars. Pillars of other shapes such as triangles and squares were also fabricated.

**Additional sample characterization.** Fig. S1(c) shows a confocal photoluminescence image of a 20 nm layer hBN on a silica pillar substrate after annealing for 30 mins at 850  $^{\circ}\text{C}$  in an argon environment at 1 Torr. The pillars have a 4  $\mu\text{m}$  pitch, are  $\sim 500$  nm in diameter and 155 nm in height. As seen in Fig. S1(c), much of the hBN film emits and thus provides evidence that the defect centers are already present in the hBN and only require activation whether via strain or through annealing. From Fig. S1(d) we find that the spectrum is comparable to the emission produced at strained locations near the pillars and suggests that both methods activate similar types of defects. The excitation source is a 460 nm cw laser. Fig. S1(e) is a confocal photoluminescence image of a multilayer hBN film on a copper substrate before transfer where preferential emission occurs at wrinkled regions of the hBN. This proves that the defects are already present in the hBN film and are not created or activated due to the transfer process. Fig. S1(f) Confocal photoluminescence image of a monolayer CVD hBN film on a pillar array where preferential emission occurs at pillar sites. Strain selective activation is seen down to the monolayer limit. The emission is found to be roughly an order of magnitude weaker than its multilayer counterpart and is highly unstable.

**Optical measurements.** All photo-luminescent measurements reported herein were collected at room temperature via a custom-built confocal microscope with an infinity-corrected 50x (.83 numerical objective) Olympus objective. The spatial resolution of the confocal microscope is 450nm. The excitation source had a spot size of 1  $\mu\text{m}$  and varied between two different lasers: a continuous wave (cw) laser operating at 460 nm (Thorlabs L462P1400MM), and a 500 fs pulse fiber laser with a repetition rate of 80 Mhz operating at 510 nm (Toptica FemtoFiber pro TVIS). A 500 nm and 550 nm long pass filters (Thorlabs FELO500 and FELO550, respectively) and a 532 nm laserline filter (Thorlabs FL532-10) with an angle-tuned  $\sim 529$  to  $\sim 625$  nm bandpass filter (Semrock TSP01) for were used to cut off the reflected laser for 460 nm excitation and 510 nm excitation, respectively, along the collection arm of the microscope. Correlation measurements were conducted via a free-space Hanbury, Brown and Twist interferometer, where a pair of time-synched (Picoquant – PicoHarp 300) APDs (MPD PDM) detected the quantum emission. An 80-20 splitter provided real-time spectral analysis; the 20% arm of the emission was steered into an iHR-320 Horiba spectrometer.

**Statistics and  $g^{(2)}(0)$  calculations.** All data used for the statistics in figure 4 were collected from the 75 nm diameter pillar array in fig. 4a and was excited by 510 nm laser at 300  $\mu\text{W}$ .  $g^{(2)}(0)$  was determined from the autocorrelation histograms (sampled in Fig. S4(a)) by taking the ratio of the area of the coincidence peak at  $t=0$  to average area of 10  $t \neq 0$  peaks, where each peak was fit with a Lorentzian function. Of the 80 pillars studied in figure 4, antibunching measurements were attempted on 45 of the pillars, where 78% of the locations had a  $g^{(2)}(0) < .8$ . Fig. S4(c) compares the number of peaks seen in a 60 second spectral time-trace (full

statistics given by fig. 4a-right side) with the maximum number of emitters determined by  $g^{(2)}(0)$  values (full statistics in fig. 4c) on each respective pillar. The maximum number of emitters,  $n$ , per pillar site determined by  $g^{(2)}(0)$  values is found by using the relation  $1 - \frac{1}{n-1} \leq g^{(2)}(0) \leq 1 - \frac{1}{n}$  [2]. We find that the average difference between both measurements is .97, where 26 of the pillar sites had a difference of 1 or less. To determine the central wavelength of an emission peak for fig. 4b, the time trace graph was integrated for the life of the emitter.

## 2. Photonic effects in pillar structures

To confirm that the quantum emission along the pillar edges is not due to photonic effects, Comsol Multiphysics was used to perform electro-magnetic finite element method (FEM) simulations of the excitation/emission efficiency in our pillar structures. The index of refraction for silica was taken to be 1.45 and the optical constants for silicon and hBN were obtained from supplementary ref. [3] and supplementary ref. [4], respectively. The dimensions used correspond to those of the sample in Figure 3, with step height of 142 nm and width of 2  $\mu\text{m}$ . From Fig. S2(a), the dipole emission is found to be maximum when the emitter is placed at the center of the pillar. This is in stark contrast with our observations in Figure 3(a) where the maximum emission is clearly at the pillar edge and shows that the origin of enhanced emission is not due to higher out-coupling from the hBN due to scattering effects along the pillar edge.

In Fig. S2(c), we rule out near-field enhancement of the excitation beam by looking at its E-field distribution for both TE and TM polarizations, at normal incidence and at an angle of incidence (AOI) of  $40^{\circ}$ , where  $53^{\circ}$  is the corresponding maximum angle of the objective. When illuminated at the edges, we find that the field strength and the confinement of the E-field varies greatly between the two polarizations. If we compare these results to the confocal PL image of the square pillars in Fig. S2(b) (vertically polarized excitation beam), we see that there is no correlation between intensity and the width of the emission with directionality of the pillar wall. Next, when we compare the field strength of the excitation beam at the pillar edge and the center, we find that the field enhancement at the edge is at most  $\sim 2x$  times higher inside the hBN while at higher AOIs, it is much less, roughly equal for TM ( $E_x$ ) polarization and 1.2x higher for TE ( $E_z$ ) polarization. These levels of enhancement cannot explain the large contrast between the fluorescence from the pillars and from flat regions of the substrate (at times exceeding 100-fold, see, e.g., Figure 2(a) in the main text). Furthermore, we do not observe any emission enhancement at the corners of the triangles and squares, expected in a photonic-dominated response.

## 3. Deformation induced charge trapping

Kirchhoff-Love (KL) theory models the static deformation of a thin plate under forces and moments [5]. The displacement of a three-dimensional plate is expressed in terms of the displacement of a two-dimensional plane, called the mid-plane. The displacement of the plate,  $\vec{u}(\vec{x})$  is written as a first order Taylor expansion around the mid-plane. The theory holds under the following assumptions: (1) the thickness of the plate does not change during deformation, (2) a line normal to the mid-surface does not bend under deformation, (3) this line also remains normal to the mid-

surface. Defining the in-plane and out-of-plane displacements of the mid-plane in cylindrical coordinates — written  $\vec{u}_{\parallel}(r, \phi)$  and  $u_{\perp}(r, \phi) \hat{z}$ , respectively — the displacement of a point in the three-dimensional plate takes the following form<sup>5</sup>:

$$\vec{u}(r, \phi, z) = \vec{u}_{\parallel}(r, \phi) - \vec{v}(zu_{\perp}(r, \phi)).$$

Derivation of the above equation invokes the small angle approximation and is, therefore, only valid for deformation angles  $< 10^{\circ}$  — which holds for the hBN plate [5]. The out-of-plane displacement of the top surface of a hBN plate is extracted from atomic force microscope (AFM) measurements. Assuming the top surface is parallel to and of uniform height above the mid plane, the AFM measurements approximate the corresponding deformation of the mid-plane (Fig. S5(a)). Given the azimuthal symmetry of the pillar, the  $\phi$  dependence can be dropped. Numerically integrating over the azimuthal angle of the data, i.e. taking radial average of the flake deformation, gives  $u_{\perp}(r)$ .

The in-plane displacement is unknown and is expected to be small due to the much greater in-plane elastic moduli of hBN [6]. It is hence assumed that the total displacement is well represented by the out-of-plane displacement alone. The displacement simplifies accordingly,

$$\vec{u}(r, z) = -\vec{v}(zu_{\perp}(r)).$$

The displacement is used to calculate the various components of strain as follows:

$$\begin{aligned} \epsilon_{rr} &= \partial_r u_r(r, \phi, z) = z \partial_r^2 u_{\perp}(r), \\ \epsilon_{\phi\phi} &= \frac{1}{r} u_r(r, \phi, z) + \partial_{\phi} u_{\phi}(r, \phi, z) = \frac{z}{r} \partial_r u_{\perp}(r), \\ \epsilon_{r\phi} &= \epsilon_{rz} = \epsilon_{zz} = \epsilon_{\phi z} = 0. \end{aligned}$$

The strain, and so the curvature of the deformation, is directly proportional to the deformation potential,  $V_{DP}(r)$ .

$$V_{DP}(r, z) = \alpha(\epsilon_{rr} + \epsilon_{\phi\phi})$$

where the deformation potential amplitude,  $\alpha$ , is different for holes and electrons. Holes are described by the deformation potential

amplitude at the valence band maximum  $\alpha_{VBM} \approx -1.64$  eV, and electrons are described by the deformation potential amplitude at the conduction band minimum  $\alpha_{CBM} \approx -4.67$  eV. These parameters were calculated by Wiktor and Pasquarelli [7] for the **K**-point of hBN. The deformation potential at the top layer of the flake and each charge carrier is depicted in Fig. S5(b). Each estimated potential is sufficient to localize electrons or holes at the lip of the pillar and vice-versa at the base.

$V_D$  depends on  $z$  linearly, and is zero along the mid plane, so it reaches its maxima or minima in  $z$  on the top and bottom surfaces of the flake. That is, where there is tensile strain on the top surface there is compressive strain on the bottom surface, and vice versa. Accordingly, the potential at the bottom surface is simply a sign inversion of Fig. S5(b). The result is presented in Fig. S5(c).

Boltzmann statistics are used to estimate the charge density confined by the deformation potential. The Boltzmann equation,  $\rho(r, z) = \rho_0 e^{-V_{DP}(r, z)/kT}$ , describes the local density of carriers and is depicted in Fig. S5(d), where  $\rho_0$  is the density in the absence of deformation. Since the flake thickness is much less than the diffraction limited spot of the confocal microscope, the confocal image depicts the fluorescence from all defects through the thickness of the flake at each lateral point. This is therefore expected to be related to the radial charge density calculated by taking the  $z$ -integral of the Boltzmann equation. Plotted in Fig. S5(d), the charge density maximum is roughly correlated to the fluorescence maximum, but not precisely. The charge carriers in hBN are still unknown, however, this indicates that both electrons and holes can be trapped by deformation potentials and have qualitatively similar distributions. The mismatch between the model and fluorescence maximum is potentially due to the failure of the mechanical model. A potential extension of this work is to apply theory of indentation with a cylindrical punch developed by Love [8]. This theory provides a better approximation in for large strains, and accounts for thinning of the flake under deformation.

---

1. K.K. Kim, A. Hsu, X. Jia, S.M. Kim, Y. Shi, M. Dresselhaus, T. Palacios, J. Kong, "Synthesis and Characterization of Hexagonal Boron Nitride Film as a Dielectric Layer for Graphene Devices", ACS Nano 6, 8583 (2012).  
2. C. Gerry and P. Knight. 2005. Introductory Quantum Optics. Cambridge university press.  
3. J. J. Sik, J. Hora, J. Humlicek, "Optical functions of silicon at elevated temperatures", J. Appl. Phys. 84, 6291 (1998).  
4. D. Golla, K. Chattrakun, K. Watanabe, T. Taniguchi, B.J. Leroy, A. Sandhu, "Optical thickness determination of hexagonal boron nitride flakes", Appl. Phys. Lett. 102, 161906 (2013).

5. J. N. Reddy, 2006. Theory and Analysis of Elastic Plates and Shells. CRC press.  
6. A. Bosak, J. Serrano, M. Krisch, K. Watanabe, T. Taniguchi, H. Kanda, "Elasticity of Hexagonal Boron Nitride: Inelastic X-Ray Scattering Measurements." Phys. Rev. B 73, 041402 (2006).  
7. J. Wiktor, Julia, A. Pasquarello, "Absolute Deformation Potentials of Two-Dimensional Materials", Phys. Rev. B 94, 245411 (2016).  
8. A. Love and E. Hough. 2013. A Treatise on the Mathematical Theory of Elasticity. Cambridge university press.

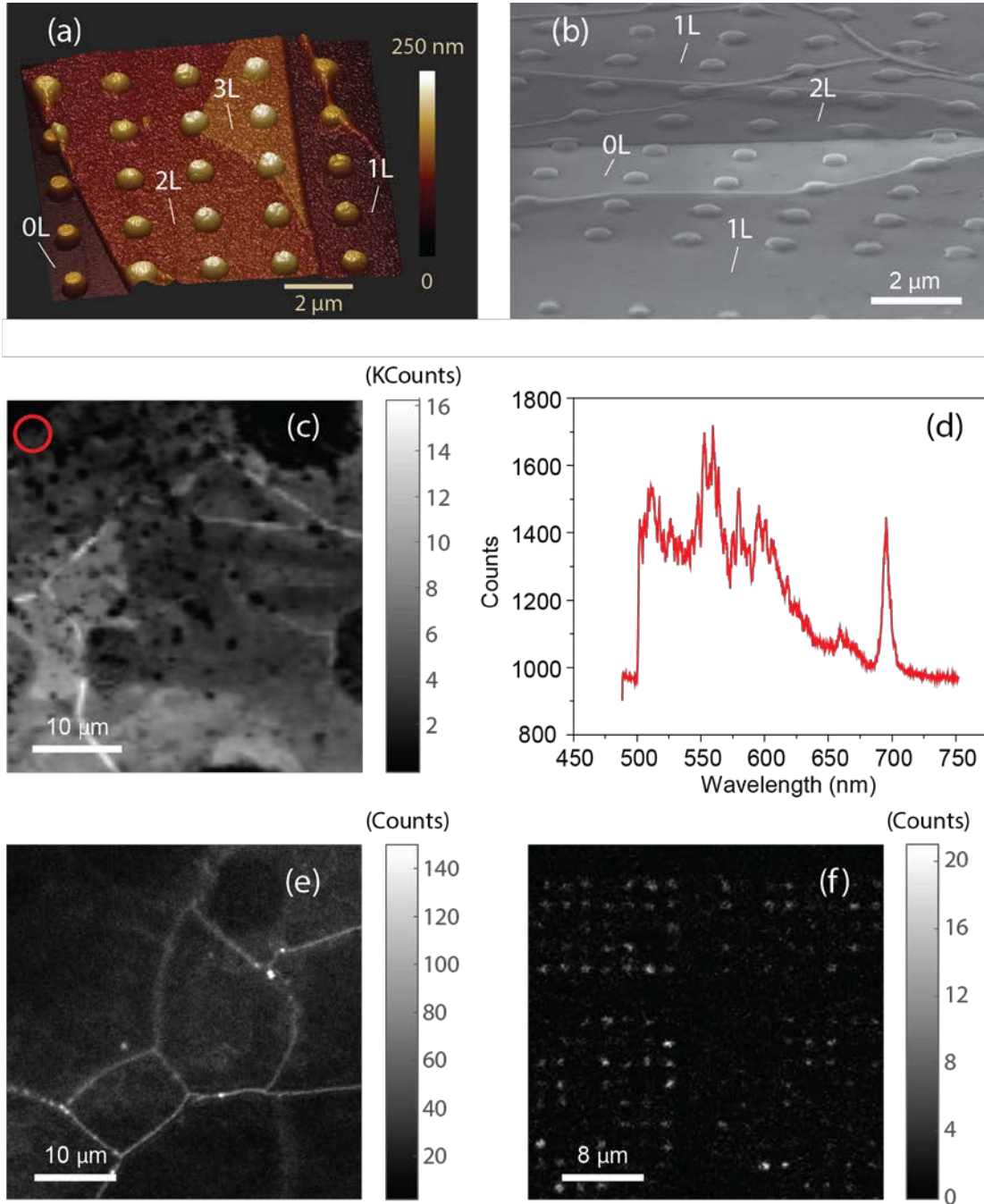


**Fig. S1 | Additional sample characterization.** (a) Tilted AFM image of 500 nm pillars with varying number of hBN layers (b) SEM image at a 70° tilt of another segment of the same region as (a). (c) A confocal photoluminescence image of a pillar sample where a significant percentage of the h-BN film emits after a 30 min anneal at 850° C. (d) A representative spectrum of the emission found in the circled area in (c). (e) Confocal photoluminescence image of as-grown multilayer hBN film on copper substrate before transfer. Preferential emission occurs at wrinkled regions of unprocessed hBN. (f) Confocal photoluminescence image of a monolayer CVD hBN film on a pillar array where preferential emission occurs at pillar sites. (a) and (b)  $nL$  with  $n:1,2,3$  denotes the number of 20-nm-thick layers;  $n=0$  corresponds to the bare substrate.

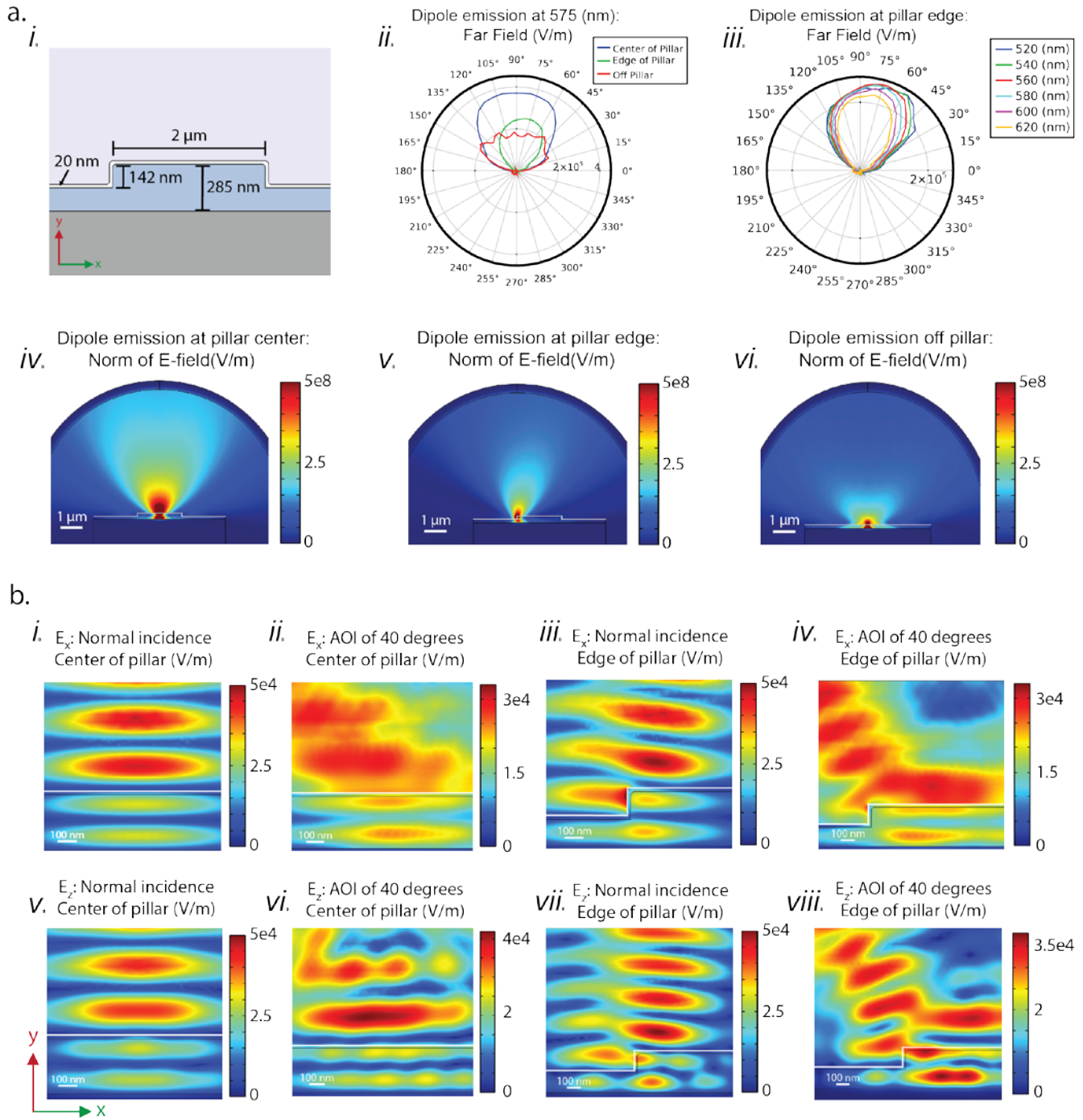


**Fig. S2 | Modeling excitation of and emission from the pillar structures.** (a) *i*) Schematic of the modeled substrate. *ii*) Far-field emission pattern of a dipole placed at the center of the pillar, edge of the pillar, and on the substrate at 575 nm. *iii*) Far-field emission profile at edge for various wavelengths. (*iv*-*vi*) Intensity plots of the electric field amplitude for the dipole locations in (a.i). (b) Intensity plots of the electric field amplitude for a 460 nm excitation beam illuminating either the center of the pillar (*i*, *ii*, *v*, *vi*) or the edge (*iii*, *iv*, *vii*, *viii*) for TM ( $E_x$ ) and TE ( $E_z$ ) polarizations. In (a) and (b) the solid white line highlights the substrate topography.

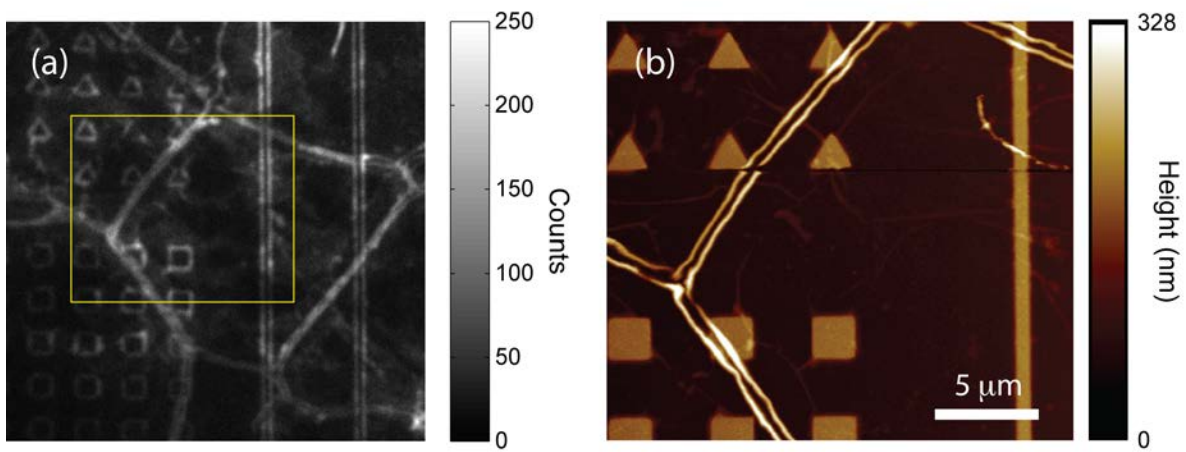


**Fig. S3 | Other structure shapes.** (a) Confocal image of hBN emission from arbitrary shapes. (c) AFM image of area within the yellow square in (b). All experimental conditions as in Figure 3.

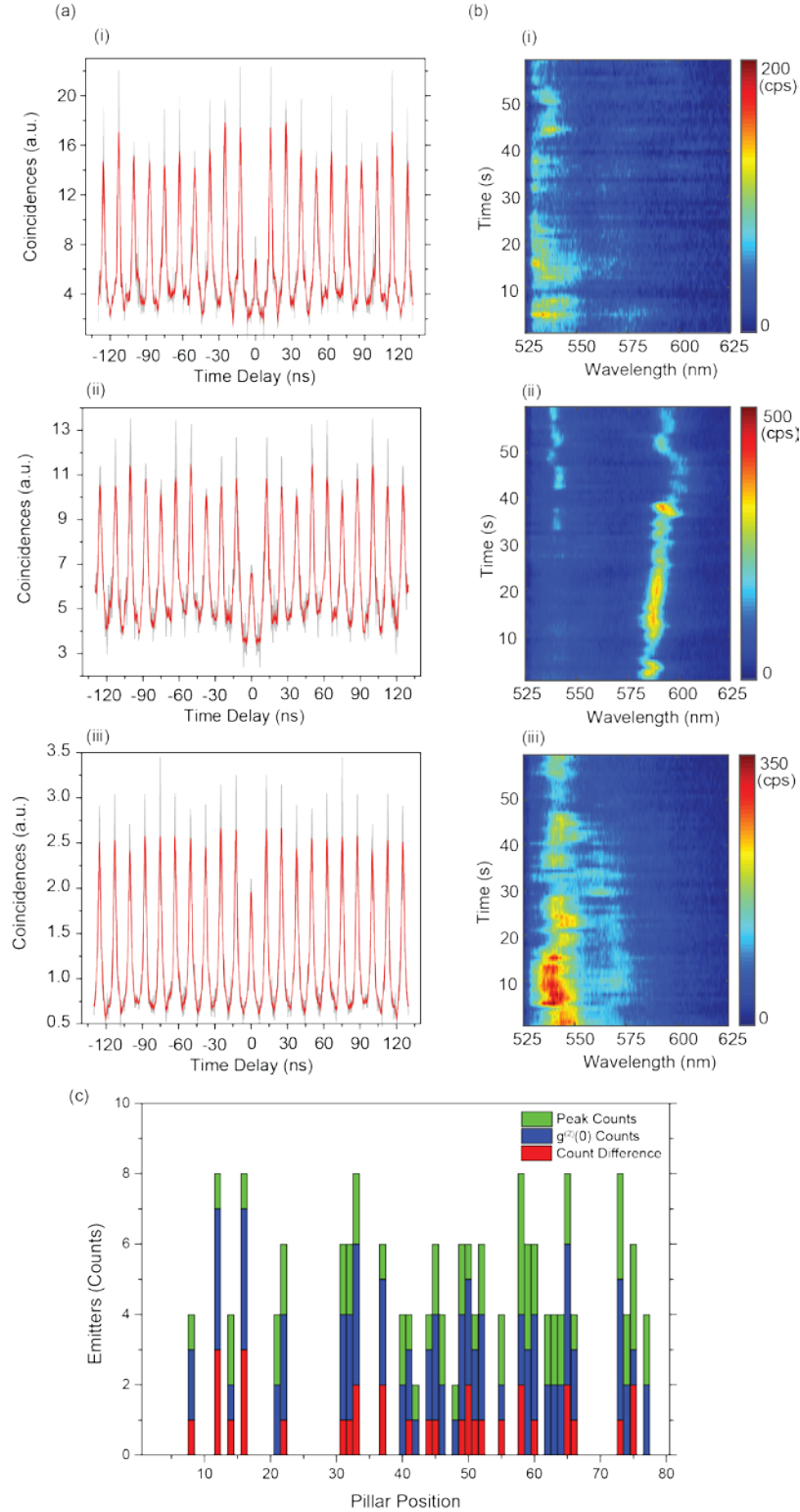


**Fig. S4 | Sample data from in figure 4.** (a) Photon correlation data and (b) complimentary spectral time-traces for (i) Pillar 2-5 (row 2-column 5) where  $g^{(2)}(0)=0.32\pm 0.02$ , (ii) Pillar 6-5 where  $g^{(2)}(0)=0.52\pm 0.04$ , (iii) Pillar 1-4 where  $g^{(2)}(0)=0.74\pm 0.04$  from fig. 4. (c) Comparison of the maximum number of emitters determined by  $g^{(2)}(0)$  and the number of emission peaks found in the respective time-trace. The pillar position is determined by stacking the columns of the array in figure 4a into an ordered list.

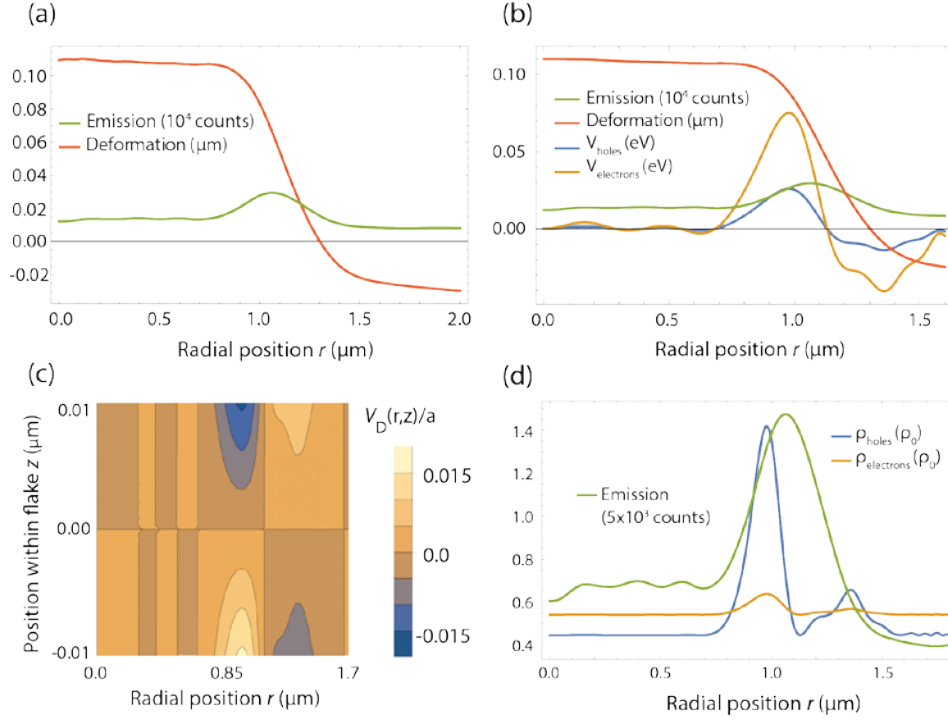


**Fig. S5 | Deformation potential for thin hBN draped over pillar.** Deformation potential calculations for hBN on the 2  $\mu\text{m}$  diameter circular pillar studied in fig. 4. (a) Measured radial deformation of a single layer hBN flake over a  $\text{SiO}_2$  the nano-pillar. (b) Calculated deformation potential on the top surface of the hBN flake. (c) Deformation potential over a plane normal to the mid-plane. (d) Radial charge localization of both electrons and holes in hBN. The electron and hole densities are in units of  $\rho_0$  which is the local density of carriers.